



Investigating decadal variations of the seasonal predictability limit of sea surface temperature in the tropical Pacific

Zhaolu Hou¹ · Jianping Li^{1,2} · Ruiqiang Ding³ · Jie Feng⁴

Received: 20 October 2021 / Accepted: 25 January 2022 / Published online: 14 February 2022
© The Author(s) 2022

Abstract

El Niño and the Southern Oscillation (ENSO) have a worldwide impact on seasonal to yearly climate. However, there are decadal variations in the seasonal prediction skill of ENSO in dynamical and statistical models; in particular, ENSO prediction skill has declined since 2000. The shortcomings of models mean that it is very important to study ENSO seasonal predictability and its decadal variation using observational/reanalysis data. Here we quantitatively estimate the seasonal predictability limit (PL) of ENSO from 1900 to 2015 using Nonlinear local Lyapunov exponent (NLLE) theory with an observational/reanalysis dataset and explore its decadal variations. The mean PL of sea surface temperature (SST) is high in the central/eastern tropical Pacific and low in the western tropical Pacific, reaching 12–15 and 7–8 months, respectively. The PL in the tropical Pacific varies on a decadal timescale, with an interdecadal standard deviation of up to 2 months in the central tropical Pacific that has similar spatial structure to the mean PL. Taking the PL of SST in the Niño 3.4 region as representative of the PL in the central/eastern tropical Pacific, there are clearly higher values in the 1900s, mid-1930s, mid-1960s, and mid-1990s, and lower values in the 1920s, mid-1940s, and mid-2010s. Meanwhile, the PL of SST in the Niño 6 region—whose average value is 7 months—is in good agreement with the PL of most regions in the western tropical Pacific, with higher values in the 1910s, 1940s, and 1980s and lower values in the 1930s, 1950s, and mid-1990s. In the framework of NLLE theory, the PL is determined by the error growth rate (representing the dissipation rate of the predictable signal) and the saturation value of relative error (representing predictable signal intensity). We reveal that the spatial structure of the mean PL in the tropical Pacific is determined mainly by the error growth rate. The decadal variability of PL is affected more by the variation of the saturation value of relative error in the equatorial Pacific, whereas the error growth rate cannot be ignored in the PL of some regions. As an important source of predictability in ENSO dynamics, the relationship between warm water volume and SST in the Niño 3.4 region has a critical role in the decadal variability of PL in the tropical Pacific through the error growth rate and saturation value of relative error. This strong relationship reduces the error growth rate in the initial period and increases the saturated relative error, contributing to the high PL.

✉ Jianping Li
ljp@ouc.edu.cn

¹ Frontiers Science Center for Deep Ocean Multispheres and Earth System (FDOMES)/Key Laboratory of Physical Oceanography/Academy of the Future Ocean/College of Oceanic and Atmospheric Science, Ocean University of China, Qingdao 266100, China

² Laboratory for Ocean Dynamics and Climate, Pilot Qingdao National Laboratory for Marine Science and Technology, Qingdao 266237, China

³ State Key Laboratory of Earth Surface Processes and Resource Ecology, Beijing Normal University, Beijing 100875, China

⁴ Department of Atmospheric and Oceanic Sciences and Institute of Atmospheric Sciences, Fudan University, Shanghai 200000, China

1 Introduction

As the strongest seasonal-to-interannual variability in the tropical Pacific, El Niño and the Southern Oscillation (ENSO) has major impacts on weather and climate in many parts of the world via the atmospheric bridge effect (Cai et al. 2020; Chen et al. 2004; Duan and Mu 2018; Li et al. 2019; Timmermann et al. 2018; Yeh et al. 2018; Zhang et al. 2021). Considerable progress has been made in the understanding and prediction of ENSO over the past few decades (Chen et al. 2004, 2015; Kirtman 2003; Latif et al. 1998; Wang et al. 2017; Xie et al. 2016; Zebiak and Cane 1987). Nevertheless, ENSO prediction remains challenging. The reliability of forecasts of ENSO events has been reported as being relatively lower in the early twenty-first century than

in the 1980s and 1990s, even with the ongoing improvement of forecast models. Decadal variations in ENSO forecasting skill have been identified in several analyses of numerical model predictions (Balmaseda et al. 1995; Chen et al. 2004; Kumar et al. 2017; Tang et al. 2008). The variation may be associated with the deficiencies of the ENSO prediction models, but it also depends strongly on ENSO predictability itself (Chen and Cane 2008; Duan and Mu 2018; Kirtman and Schopf 1998; Tang et al. 2008).

Many previous studies have examined decadal variations in ENSO predictability (Duan et al. 2018; Kirtman and Schopf 1998; Tang et al. 2008; Zhao et al. 2016; Zheng et al. 2016) using two common approaches: the diagnostic approach and the prognostic approach. The prognostic approach is based on hindcast experiments and widely used to explore ENSO predictability (Kirtman and Schopf 1998; Latif et al. 1998; Tang et al. 2008). The diagnostic approach uses the signal-to-noise ratio. The variance of a variable is decomposed into a signal component—which is potentially predictable—and an unpredictable noise component (Lopez and Kirtman 2014). Potential predictability at a given scale is analyzed using the ratio of the signal variance to the noise variance. However, for the signal-to-noise method, determining which part of the variance is signal and which part is noise remains somewhat subjective. This method can only qualitatively give the relative size of the predictability, not the predictability limit (PL) (Chen et al. 2006). In the prognostic approach, the predictability is estimated from the prediction skill of dynamical models and is usually model-dependent (Tang et al. 2008). These studies have significantly improved our understanding of ENSO predictability. However, forecast models are always imperfect analogs of the real ENSO dynamical system, which leads to some uncertainties in estimating ENSO predictability. Conclusions on ENSO predictability using the prognostic approach may give a rather confusing explanation of the decadal variations in ENSO forecast skill (Duan and Mu 2018). The predictability of the real ENSO system is concealed in the observational/reanalysis dataset. Thus, challenges remain in ENSO predictability studies in eliminating the negative impact of model deficiencies, deriving robust and general conclusions directly from the observational dataset, and quantitatively obtaining the PL.

The nonlinear local Lyapunov exponent (NLLE) method has been introduced to investigate atmospheric and oceanic predictability using observational data (Ding and Li 2007; Ding et al. 2008, 2016; Hou et al. 2018a; Li and Wang 2008; Li and Ding 2011, 2013, 2015; Li et al. 2018). As a nonlinear extension of the traditional Lyapunov exponent concept, the NLLE measures the nonlinear growth rate of the initial error of a nonlinear dynamical model (Chen et al. 2006). With the NLLE and its derivatives, the limit of atmospheric and oceanic predictability over various timescales can be determined quantitatively by exploring the evolution of the distance between

initially local dynamical analogs (LDA) from the observational time series (Li and Ding 2011). Therefore, the ENSO PL can be assessed using the NLLE method with observational/reanalysis data (Hou et al. 2018b). In this paper, we use the NLLE method to estimate the seasonal PL of sea surface temperature (SST) in the tropical Pacific and investigate its decadal variation. The different key Niño regions will be considered, and the performances of their decadal variations of PL are explained from the perspective of error growth dynamics.

This paper is structured as follows: Sect. 2 briefly introduces the NLLE method and describes the data used in this study. Section 3 first examines the decadal variation of SST predictability in the tropical Pacific from 1900 to 2015, then Sect. 3.2 analyzes the error growth represented by the NLLE. The possible mechanisms responsible for the decadal variations in ENSO predictability are discussed in Sect. 3.3. A summary and discussion are given in Sect. 4.

2 Method and data

2.1 The NLLE method

An n -dimensional nonlinear dynamical system is described by

$$\frac{d}{dt}\mathbf{x} = \mathbf{F}(\mathbf{x}), \quad (1)$$

where \mathbf{F} denotes the dynamical system and $\mathbf{x} = [x_1(t), x_2(t), \dots, x_n(t)]^T$ is the state vector at the time t . The evolution of an error $\boldsymbol{\delta} = [\delta_1(t), \delta_2(t), \dots, \delta_n(t)]^T$, superimposed on a state \mathbf{x} , is given by the equation:

$$\frac{d}{dt}\boldsymbol{\delta} = \mathbf{J}(\mathbf{x})\boldsymbol{\delta} + \mathbf{G}(\mathbf{x}, \boldsymbol{\delta}), \quad (2)$$

where $\mathbf{J}(\mathbf{x})$ is the tangent linear evolutionary operator and $\mathbf{G}(\mathbf{x}, \boldsymbol{\delta})$ is the high-order nonlinear term. There are some difficulties in solving the nonlinear term, so in most previous studies the initial perturbations were assumed to be sufficiently small for their evolution to be approximated by the tangent linear model of the nonlinear dynamical system (Eckmann and Ruelle 1985; Karamperidou et al. 2014; Lorenz 1969). However, the tangent linear approximation has many limitations in predictability problems involving finite-amplitude initial errors (Ding and Li 2007; Lacarra and Talagrand 1988; Li and Ding 2011; Mu and Duan 2003). Therefore, the nonlinear behavior of error growth should be considered. Without making the linear approximation, solutions of Eq. (2) can be obtained by numerical integration from $t = t_0$ to t_i ,

$$t_i = t_0 + \tau,$$

$$\delta(t_i) = \eta(\mathbf{x}(t_0), \delta(t_0), \tau)\delta(t_0), \tag{3}$$

where $\eta(\mathbf{x}(t_0), \delta(t_0), \tau)$ represents the error propagator. The definition of the NLE is:

$$\lambda(\mathbf{x}(t_0), \delta(t_0), \tau) = \frac{1}{\tau} \ln \frac{\|\delta(t_i)\|}{\|\delta(t_0)\|}, \tag{4}$$

where $\lambda(\mathbf{x}(t_0), \delta(t_0), \tau)$ is a function of the initial state $\mathbf{x}(t_0)$, the initial error $\delta(t_0)$, and the evolution time increment τ . The NLE measures the nonlinear growth rate of the initial errors of a dynamical model without linearizing the model's governing equations. For a specific class of states Ω , the ensemble average NLE, obtained by averaging $\lambda(\mathbf{x}(t_0), \delta(t_0), \tau)$,

$$\bar{\lambda}(\Omega, \delta, \tau) = \frac{\int_{\mathbf{x} \in \Omega} \lambda(\mathbf{x}(t_0), \delta(t_0), \tau) d\mathbf{x}}{\int_{\mathbf{x} \in \Omega} 1 d\mathbf{x}} = \lambda(\mathbf{x}, \delta, \tau)_{\mathbf{x} \in \Omega} = \frac{1}{\tau} \ln \frac{\|\overline{\delta(t_i)}\|_{\mathbf{x} \in \Omega}}{\|\overline{\delta(t_0)}\|_{\mathbf{x} \in \Omega}} \tag{5}$$

where $\langle \rangle_{\mathbf{x} \in \Omega}$ denotes the ensemble average of state sample set Ω and $_{\mathbf{x} \in \Omega}$ represents the geometric mean of the errors from state sample set Ω . The ensemble mean NLE reflects the evolution of mean error growth and can represent the predictability of the specific set. Based on the definition of NLE, the mean relative growth of the initial error (RGIE, $\ln \bar{E}$) may be obtained from,

$$\ln \bar{E}(\mathbf{x}, \delta, \tau) = \left[\bar{\lambda}(\Omega, \delta, \tau) \tau \right] = \ln \frac{\|\overline{\delta(t_\tau)}\|_{\mathbf{x} \in \Omega}}{\|\overline{\delta(t_0)}\|_{\mathbf{x} \in \Omega}}. \tag{6}$$

The concept of RGIE can be extended as the mean relative growth during a specific period. Considering the period from τ_i to τ_j , the mean relative growth may be written:

$$\ln \bar{E}(\mathbf{x}, \delta, \tau_i \rightarrow \tau_j) = \ln \bar{E}(\mathbf{x}, \delta, \tau_j) - \ln \bar{E}(\mathbf{x}, \delta, \tau_i) = \ln \frac{\|\overline{\delta(t_{\tau_j})}\|_{\mathbf{x} \in \Omega}}{\|\overline{\delta(t_{\tau_i})}\|_{\mathbf{x} \in \Omega}} \tag{7}$$

According to dynamical systems error growth theory, $\bar{E}(\mathbf{x}, \delta, \tau)$ will converge to a saturation level with increasing τ (Ding and Li 2007). Using the theoretical saturation level, the predictability limit can be quantitatively determined (Ding and Li 2007; Li and Ding 2011). The RGIE grows with increasing evolution time and reaches the saturation error level when the information from the initial state is completely lost; this evolution time is regarded as the PL. A schematic illustration of the determination of

the PL using the NLE method is shown as Fig. 1 in Ding et al. (2016).

For dynamical systems, whose governing equations are known explicitly, the mean NLE and RGIE may be calculated directly by numerical integration of their error evolution equations (Ding and Li 2007). However, the dynamical equations of the atmosphere and ocean are explicitly unknown, but abundant observational/reanalysis data are available, so we can estimate the mean NLE by using these data with the local dynamical analog (LDA) method (Hou et al. 2020, 2021; Li and Ding 2011). The general purpose of the LDA method is to find the analogues for each base trajectory from the observational time series based on initial and evolved features at two different states (time points) in the time series, then estimate the exponential divergence rate between the base trajectories and their analogues as the

NLE. The mean RGIE can also be calculated. To reduce the effect of error fluctuations, the predictability limit in this study is defined as the time at which the error reaches 95% of its saturation value. The saturation value is obtained by taking the average of the mean error growth after the error almost stops increasing, following the work of Ding et al. (2016). More detailed descriptions and a derivation of the NLE and LDA method can be found in Li and Ding (2011) and Ding et al. (2016).

Data in geophysical time series always have a certain persistence and are not completely independent. Thus, the effective degrees of freedom for the samples must be considered when computing statistics (Bretherton et al. 1999). In this method, the effective degrees of freedom for significance tests with autocorrelations sequences $\rho_{XX}(j)$ and $\rho_{YY}(j)$ are derived as follows (Li et al. 2013, 2021; Pyper and Peterman 1998):

$$\frac{1}{N^{eff}} \approx \frac{1}{N} + \frac{2}{N} \sum_{j=1}^{N-2} \frac{N-j}{N} \rho_{XX}(j) \rho_{YY}(j), \tag{8}$$

where N^{eff} is the effective number of degrees of freedom used in the significance calculation, N is the sample size (unadjusted number of degrees of freedom), and $\rho_{XX}(j)$ and $\rho_{YY}(j)$ are the autocorrelations of two sampled time series X and Y at time lag j , respectively.

2.2 Data

The monthly SST dataset used in this study is version 5 of the Extended Reconstructed SST (ERSST.v5) generated by the National Oceanic and Atmospheric Administration (NOAA) on a $2^\circ \times 2^\circ$ spatial grid (Huang et al. 2017), covering the period January 1854 to December 2019. The associated subsurface ocean temperatures were investigated using the Simple Ocean Data Assimilation dataset (SODA; available online at <http://www.atmos.umd.edu/~ocean/>). Version 2.2.4 of the SODA dataset consists of monthly-mean data spanning 1871–2008 with $0.5^\circ \times 0.5^\circ$ horizontal resolution. The monthly mean ocean temperature data from The National Center for Environmental Prediction Global Ocean Data Assimilation System from January 1979 to the present are also used (GODAS; Behringer 2007). Using the ocean temperature and depth of the 20°C isotherm (D20) from both SODA and GODAS, a warm water volume (WWV) index is defined as the average of D20 over the region 5°S – 5°N , 120°E – 80°W (Meinen and McPhaden 2000). The WWV index from GODAS and that from SODA are normalized separately, and have good consistency in their common periods. Therefore, we produced a new WWV index by combining that from SODA before 2008 and from GODAS since 2008 to the present.

Before calculating the PL, the climatological mean annual cycle and quadratic trend were first removed from the SST data to obtain the sea surface temperature anomaly (SSTA) at each grid point. The quadratically detrended process is expected to reduce the effects owing to global warming. To extract the seasonal to interannual components of the SSTA, a 9-year high-pass Gaussian filter is applied. The PL and RGIE at each grid point can be determined from the SSTA time series by applying the NLLE method. The mean NLLE and RGIE are calculated using a $(9 \times 12 + 1)$ -month moving window from 1900 to 2019. The moving window moves forward every month. The time axis indicates the middle month of the $(9 \times 12 + 1)$ month moving window. The seasonal predictability limit of SSTA for different decades is estimated from the mean NLLE. To highlight the decadal component, a 9-year high-pass Gaussian filter is applied to the monthly PL. We also use other SST datasets (OISST, Hadley and Kaplan SST; Kaplan et al. 1998; Rayner et al. 2003; Reynolds et al. 2007), with different moving windows (from 7- to 13-year), and the results are similar.

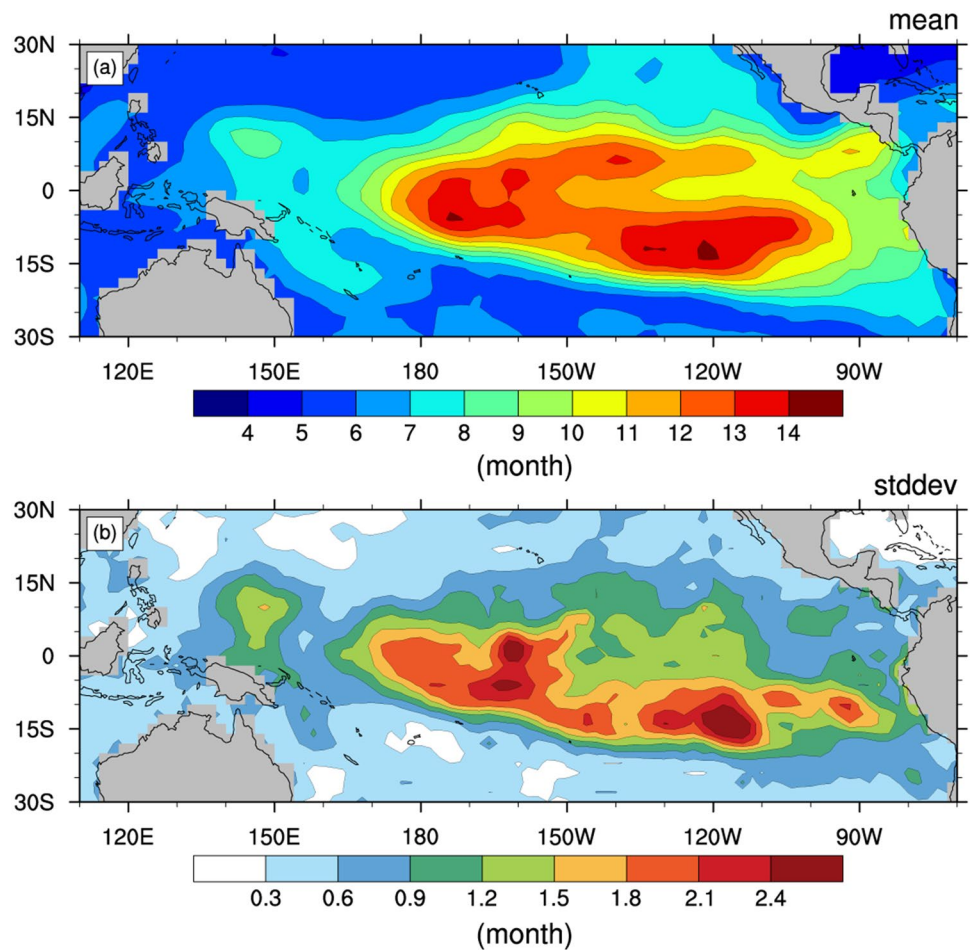
3 Results

3.1 Predictability limit of the tropical Pacific

The spatial distribution of the mean PL of monthly SST from 1900 to 2015 over the tropical Pacific is shown in Fig. 1a. The mean PL over the tropical and subtropical Pacific (110°E – 70°W , 30°S – 30°N) is 6.95 months. Zonally averaged, the PL in the equatorial Pacific is higher than that off the equator. From east to west along the equatorial Pacific, the PL in the central and eastern Pacific (exceeding 12 months) is relatively higher than that in the western tropical Pacific (5–7 months). The highest PL (> 14 months) is in the region east of the equatorial international dateline, and another high PL region (> 13 months) occurs in the South Pacific cold tongue off the equator (SPT; 5°S – 15°S , 140°W – 100°W). Of the different Niño key regions, the PL is the highest in the Niño 3.4 region (5°S – 5°N , 170°W – 120°W ; > 12 months), followed by the Niño 3 region (5°S – 5°N , 150°W – 90°W ; 10–13 months), and then the Niño 1 + 2 region (10°S – 0° , 90°W – 80°W ; 8–9 months); these values are consistent with the results of Li and Ding (2013). The spatial structure of the PL in the tropical Pacific at seasonal to interannual time scales is associated with the ENSO dynamics system. The regions related to the ENSO oceanic process have relatively high PL, such as the Niño key regions—including Niño 6 region (8°N – 16°N , 140°E – 160°E)—implying the important role of the ENSO mechanism in the predictability of SSTA through the physical processes described by the delayed oscillator and recharge–discharge theory (Jin 1997; Wang et al. 1999; Wang 2018; Wyrski 1985).

Tang et al. (2008) performed ENSO hindcasts from 1881 to 2000 and highlighted that the prediction skill for different dynamical models showed consistent interdecadal variation; this is the decadal variation of ENSO predictability represented by SST from models rather than the real physical system. In Fig. 2, we display the decadal variation of the mean PL from observational/analysis data in several key Niño regions and the SPT region. The curves in Fig. 2 are the seasonal PLs of SST under a $(9 \times 12 + 1)$ -month-low-pass filter and reflect the variation of seasonal predictability in different decades. The mean PL over the period from 1900 to 2015 is highest in the SPT (13.2 months) and Niño 3.4 (12.0 months) regions, followed by the Niño 4 (11.4 months) and Niño 3 (11.0 months), Niño 1 + 2 (8.9 months), and Niño 6 (7.3 months) regions, and lastly by the Niño 5 region (6.2 months), which is consistent with the values shown in Fig. 1. The PLs in these regions show decadal variation. The standard deviation over the period from 1900 to 2015 reflects the magnitude of decadal variation; in the SPT (1.40 months), Niño 3.4 (1.17 months), and Niño 4 (1.37 months) regions it is higher than that

Fig. 1 **a** Spatial distribution of the mean seasonal predictability limit (PL) of SST and **b** its standard deviation on the decadal scale over the tropical Pacific from January 1900 to December 2015

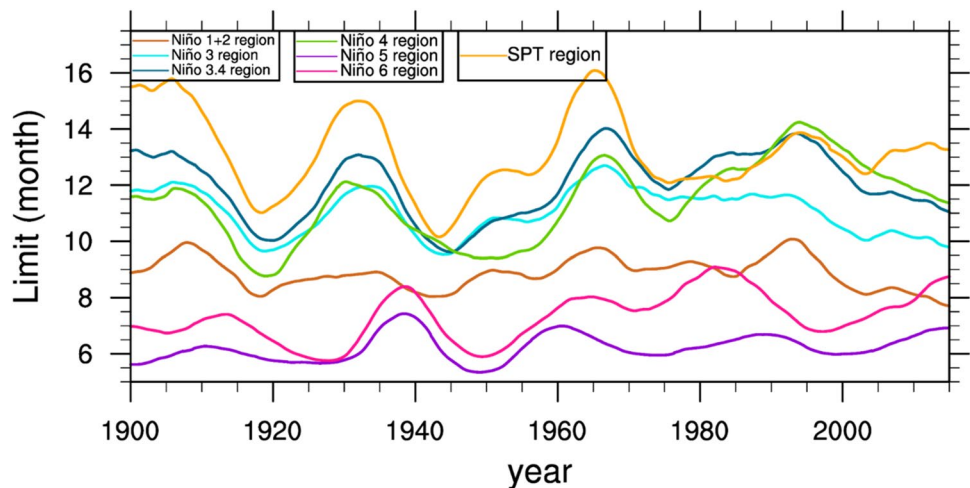


in the Niño 3 (0.83 months) and Niño 6 (0.87 months) regions. The decadal variation in the Niño 1 + 2 region is 0.56 months, and the lowest variation occurs in the Niño 5 region (0.47 months).

The spatial features of decadal variability of the PL are shown in terms of the standard deviation on a decadal scale

of the seasonal PL in each grid cell of the tropical Pacific in Fig. 1b. Its spatial distribution is consistent with that of Fig. 1a, and there is larger variability in the equatorial region than in the off-equator regions. The mean standard deviation over the whole tropical Pacific is 1.08 months. The maximum values (> 2.4 months) are found in the central tropical

Fig. 2 Decadal variation of the seasonal PL in the Niño 1 + 2 region (10° S–0°, 90°–80° W; brown), Niño 3 region (5° S–5° N, 150°–90° W; cyan), Niño 3.4 region (5° S–5° N, 170°–120° W; deep-sky-blue), Niño 4 region (5° S–5° N, 160°E–150°W; green), Niño 5 region (5° S–5° N, 120° E–140° E; dark violet), Niño 6 region (8°–16° N, 140° E–160° E; deep pink), the South Pacific cold tongue off the equator (SPT region; 5°–15° S, 140°–100° W; orange)



Pacific (5° S–5° N, 170° E–150° W) and the SPT region off the equator. The decadal variation of the seasonal PL in the central Pacific is larger than that in the eastern and western Pacific, consistent with the results in Fig. 2. Relative to the subtropical regions and western tropical Pacific regions, the PL decadal variability in the Niño 6 region is high, which implies the important role of ENSO dynamical processes in the PL of SST.

The seasonal PLs in the central and eastern tropical Pacific regions share some features of decadal variation. As shown in Table 1, the correlation coefficients between the PLs in the Niño 1 + 2 region and in the Niño 3, Niño 3.4, and Niño 4 regions are 0.84, 0.73, and 0.46, respectively, all of which reach the 90% confidence level. The correlation coefficients between Niño 3, Niño 3.4, and Niño 4 are all greater than 0.5 and significant at the $\alpha = 0.1$ level. The high correlation coefficients between the PL curves of the Niño 1 + 2, 3, 3.4, and 4 regions suggest that the same oceanic and atmospheric processes contribute to the PL of SST in the central and eastern Pacific. Interestingly, the decadal variability of the PL in the western tropical Pacific has relatively low consistency with that in the central and eastern Pacific. The PLs of the western Pacific, such as the Niño 5 and 6 regions, have low correlation with those of other Niño regions (Table 1). However, the PLs in the Niño 5 and 6 regions, whose SSTs are representative of those in the western Pacific, have highly consistent decadal variability.

Considering the difference in PL between the western and central/eastern Pacific, we choose the Niño 3.4 region to represent the central/eastern Pacific and the Niño 6 region for the western Pacific. The correlation coefficient between the PL in the Niño 3.4 region and PLs over the tropical Pacific is shown in Fig. 3a. Dotted regions indicate where the correlation coefficients pass the 90% confidence level. As mentioned above, the PL of the central and eastern tropical Pacific agrees well with the decadal variability of the PL of the Niño 3.4 region. However, the PLs of the western tropical and subtropical Pacific

have low correlation with the decadal variability of the PL of the Niño 3.4 region. Figure 3b shows the correlation pattern between the PL of the Niño 6 region and those over the tropical Pacific. There is significant correlation in the western Pacific, where the PLs have insignificant correlation with those of the central/eastern Pacific, such as in the Niño 3.4 region. Thus, the results of Table 1 and Fig. 3 imply that the decadal variation of the PL in the central/eastern tropical Pacific is inconsistent with that in the western tropical and subtropical Pacific, and the decadal variation of the PLs in the Niño 6 and Niño 3.4 regions can be regarded as representative of that in the central/eastern, and western tropical Pacific, respectively.

In the central/eastern tropical Pacific, the PLs in the Niño 3.4 region have larger values (> 13 months) in the early 1900s, mid-1930s, mid-1960s and mid-1990s, along with lower values (< 11 months) around the 1920s, mid-1940s and mid-2010s, as shown in Fig. 2. Since the mid-1990s, the PLs in the Niño 1 + 2, 3, 3.4, and 4 regions have declined, as verified by the reduced forecast accuracy in ENSO operational models (Barnston et al. 2012; Zhao et al. 2016; Zheng et al. 2016). In contrast to the decadal variation of the PL in the Niño 3.4 region, the larger PLs (> 7.0 months) of the Niño 6 region in the western Pacific appear in the mid-1910s, 1940s, mid-1980s and mid-2010s. The PLs of the Niño 6 region are lower (< 7.0 months) in the 1930s, 1950s and mid-1990s. Interestingly, the PLs in the Niño 5 and 6 regions have increased since the mid-1990s. In fact, the model forecast skill from the North American Multi-Model Ensemble performs better in the western tropical Pacific since mid-1990s.

More detail of the decadal variability of the equatorial Pacific is shown in the longitude–time evolution of PL in the equatorial Pacific (5° S–5° N) in Fig. 4. The average PLs for different longitudes show that the seasonal PL is larger in the eastern and central tropical Pacific than in the western tropical Pacific, and the highest PLs (~ 14 months) are found from 180° to 150°W, consistent with Figs. 1 and 2. In addition to the lowest PL, seen in the western tropical

Table 1 Correlation coefficients between the decadal variations of seasonal PLs in different Niño regions from 1900 to 2015. Niño 1 + 2 region (10° S–0°, 90°–80° W), Niño 3 region (5° S–5° N, 150°–90°

W), Niño 3.4 region (5° S–5° N, 170°–120° W), Niño 4 region (5° S–5° N, 160° E–150° W), Niño 5 region (5° S–5° N, 120° E–140° E), Niño 6 region (8°–16° N, 140° E–160° E)

Niño region	1 + 2	3	3.4	4	5	6
1 + 2	1.00	0.84**	0.73**	0.46*	– 0.02	0.04
3		1.00	0.86**	0.51*	0.11	0.25
3.4			1.00	0.85**	0.18	0.34
4				1.00	0.28	0.38
5					1.00	0.74**
6						1.00

** and * denote significant correlations at the 95% and 90% confidence levels, respectively

Fig. 3 Spatial field over the tropical Pacific of PL correlation with those over the **a** Nino 3.4 and **b** the Nino 6 regions. The dotted region represents correlation coefficients exceeding the 90% confidence level

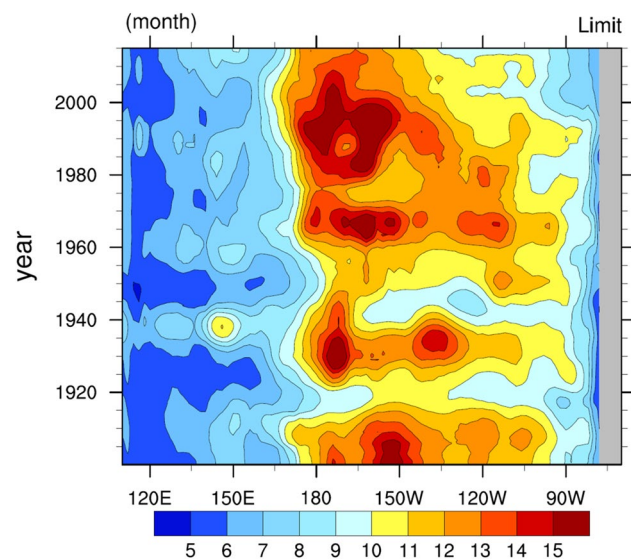
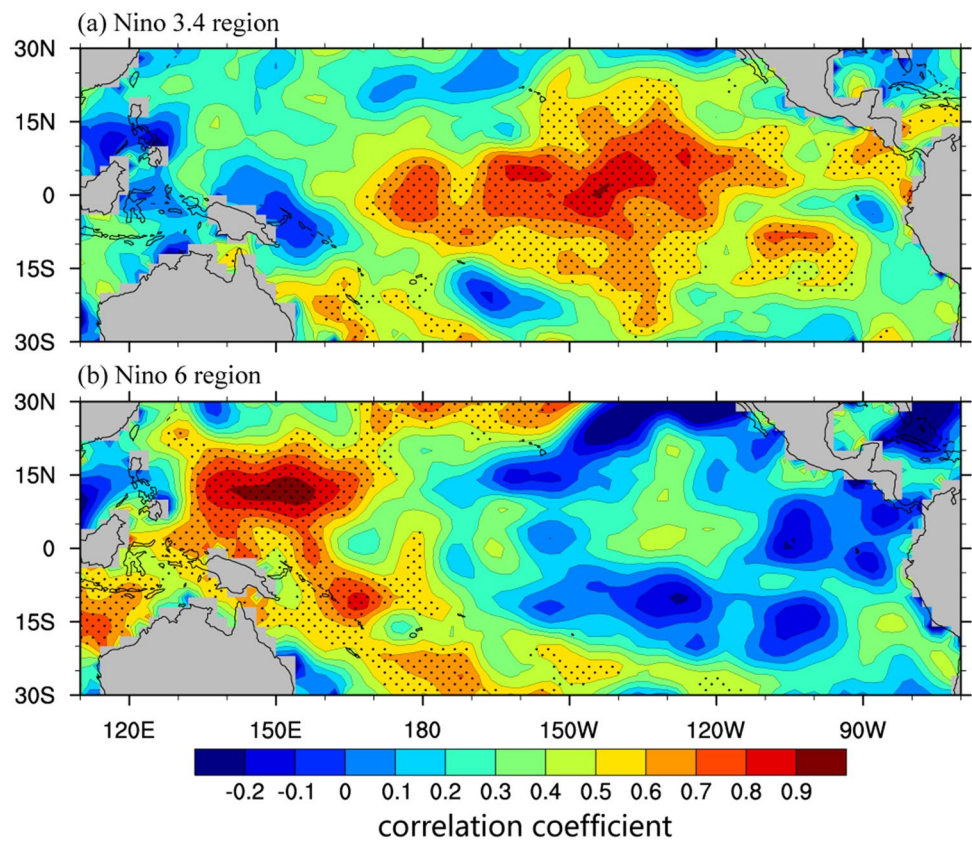


Fig. 4 Hovmöller diagram of the predictability limit zonally averaged from 5° S to 5° N in the tropical Pacific. The ordinate is the time from 1900 to 2015 and the abscissa is the longitude from 110° E to 70° W

Pacific, there are low PL values (< 8 months) east of 90° W from 1900 to 2015, which may be due to the influence of offshore current processes. The different values of the PL in the western, central, and eastern Pacific mean that the zonal

gradient of PL in the tropical Pacific changes with longitude. Relative to other longitude regions, the zonal gradient of PL is larger near 170° E, which is a key area of air–sea coupling including wind divergence and the zonal advection of SST in ENSO dynamics.

Like the decadal variation described by the PL curves in Niño regions shown in Fig. 2, the decadal variability of the PL for the whole tropical Pacific in Fig. 4 is more evident in certain decades. The PLs for almost all of the equatorial Pacific are lower in the 1920s and mid-1940s. The high PL areas (> 14 months) from 180° W to 150° W also vary on a decadal basis and occur mainly in the 1900s, mid-1930s, mid-1960s and mid-1990s. The central longitudes of the high PL areas also differ with decade; for example, 150° W in the 1900s, 170° W in the mid-1930s, and 160° W in the mid-1960s and mid-1990s. The high PL areas (> 14 months) in the central and eastern equatorial Pacific are larger and more sustained in the period from the 1980s to 2000s. The decline of the PL in the tropical Pacific since the mid-1990s occurs mainly in the central and eastern Pacific and corresponds to a reduction in the area where PL is greater than 11 months. The reduction of the high PL toward the central Pacific started in the mid-1990s and is ongoing. Meanwhile, the PL in the western tropical Pacific has increased since the mid-1990s, and this is more obvious near 150° E. The region with PL > 8 months has expanded from 140° E to 130° E near the eastern border.

Compared with the low PL period of the 1920s and mid-1940s in the tropical Pacific, the PL decline in the central tropical Pacific since the 2000s is slightly weaker but has lasted longer.

3.2 Error growth in the tropical Pacific

From the perspective of error growth dynamics, the PL depends on the growth rate of the initial error and the error saturation level. The error saturation level represents the signal intensity, and the error growth rate determines how long the initial error takes to reach an error saturation value. Therefore, we focus on the error growth estimates from NLE, such as $\bar{\lambda}(\Omega, \delta, \tau)$ and $\ln \bar{E}(\mathbf{x}, \delta, \tau)$, to clarify the reasons for the spatial pattern and decadal variation of the seasonal PL in the tropical and subtropical Pacific.

Figure 5 shows the mean error growth values as a function of evolution time, represented by NLE, RGIE, and the errors in the Niño 3.4 and Niño 6 regions from 1900 to 2015. The mean PL in the Niño 3.4 region (12.0 months) is larger than that in the Niño 6 region (7.3 months). As a measure of

error growth rate, the NLE $\bar{\lambda}(\Omega, \delta, \tau) = \frac{1}{\tau} \ln \frac{\|\delta(\tau)\|_{\mathbf{x} \in \Omega}}{\|\delta(t_0)\|_{\mathbf{x} \in \Omega}}$ and represents the logarithmic growth rate of error relative to initial error during a period of evolution. As shown in Fig. 5a, the NLE in the Niño 6 region is always larger than that in the Niño 3.4 region over evolution periods from 1 to 10 months, which implies that the initial error grows faster in the Niño 6 region than in the Niño 3.4 region. Initial information is lost more rapidly with increasing evolution time in the Niño 6 region, which corresponds to the low PL. The RGIE or $\ln \bar{E} = \ln \frac{\|\delta(\tau)\|_{\mathbf{x} \in \Omega}}{\|\delta(t_0)\|_{\mathbf{x} \in \Omega}}$ and represents the error size relative to an initial error as a function of evolution period. The RGIE values in the Niño 3.4 and Niño 6 regions are shown in Fig. 5b. The RGIE values increase with increasing evolution time and reach the saturation level. The RGIE of the Niño 3.4 region is lower than that of the Niño 6 region and grows more slowly over the evolution time from 1 to 10 months. The dashed lines indicate the PL of the Niño 3.4 and Niño 6 regions, showing the period when the RGIE grows to the saturation level (95%). It is interesting that the saturation level of RGIE in the Niño 6 region is almost equivalent to that in the Niño 3.4 region, although the standard deviation of SST in the two regions is quite different. As well as the relative error described by $\ln \bar{E}(\mathbf{x}, \delta, \tau)$, the actual error values in both regions also grow with increasing evolution time and reach saturation levels, as shown in Fig. 5c. The error values in the Niño 6 region are always lower but grow faster and reach the saturated error level earlier than those in the Niño 3.4 region. The actual saturated error level is almost proportional to the standard deviation of the system (Li et al. 2018). The higher standard deviation and lower error growth rate in the Niño 3.4 region contribute to the higher PL compared with that in the Niño 6 region. Note, however, that high standard deviation of SST does not correspond exactly to high PL.

Figure 6b shows the spatial pattern of the actual saturated error level in the tropical Pacific over the period 1900–2015, which is very similar to the spatial pattern of the SST standard deviation. The actual errors at the saturation time are high ($> 0.7 \text{ }^\circ\text{C}$) in the central/eastern equatorial Pacific, and low ($< 0.4 \text{ }^\circ\text{C}$) in the western and subtropical Pacific. The initial error (Fig. 6a) ranges from 0.008 to 0.04 $^\circ\text{C}$ over the whole tropical Pacific, which is reasonable due to the constraint of adjacent states in phase space from the NLE theory (Castro et al. 2008; Penland and Sardeshmukh 1995; Reynolds and Smith 1994). The initial error presents a similar spatial pattern to the error saturation level pattern, as the SST standard deviation pattern not only determines the spatial pattern of the saturated error value but also affects the spatial mode of the initial error. However, the differences between the spatial pattern of the actual error and that of the mean PL are large; for example, the maximum of the error

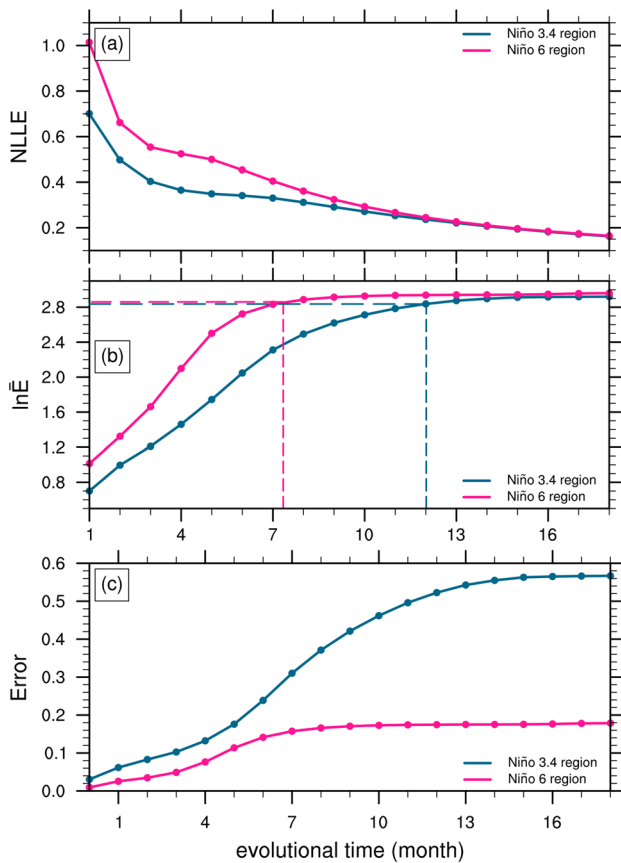


Fig. 5 Error growth in the Niño 3.4 (blue) and Niño 6 (pink) regions averaged from 1900 to 2015: **a** NLE, **b** mean relative growth of the initial error (RGIE, $\ln \bar{E}(\mathbf{x}, \delta, \tau)$), **c** actual error values ($^\circ\text{C}$)

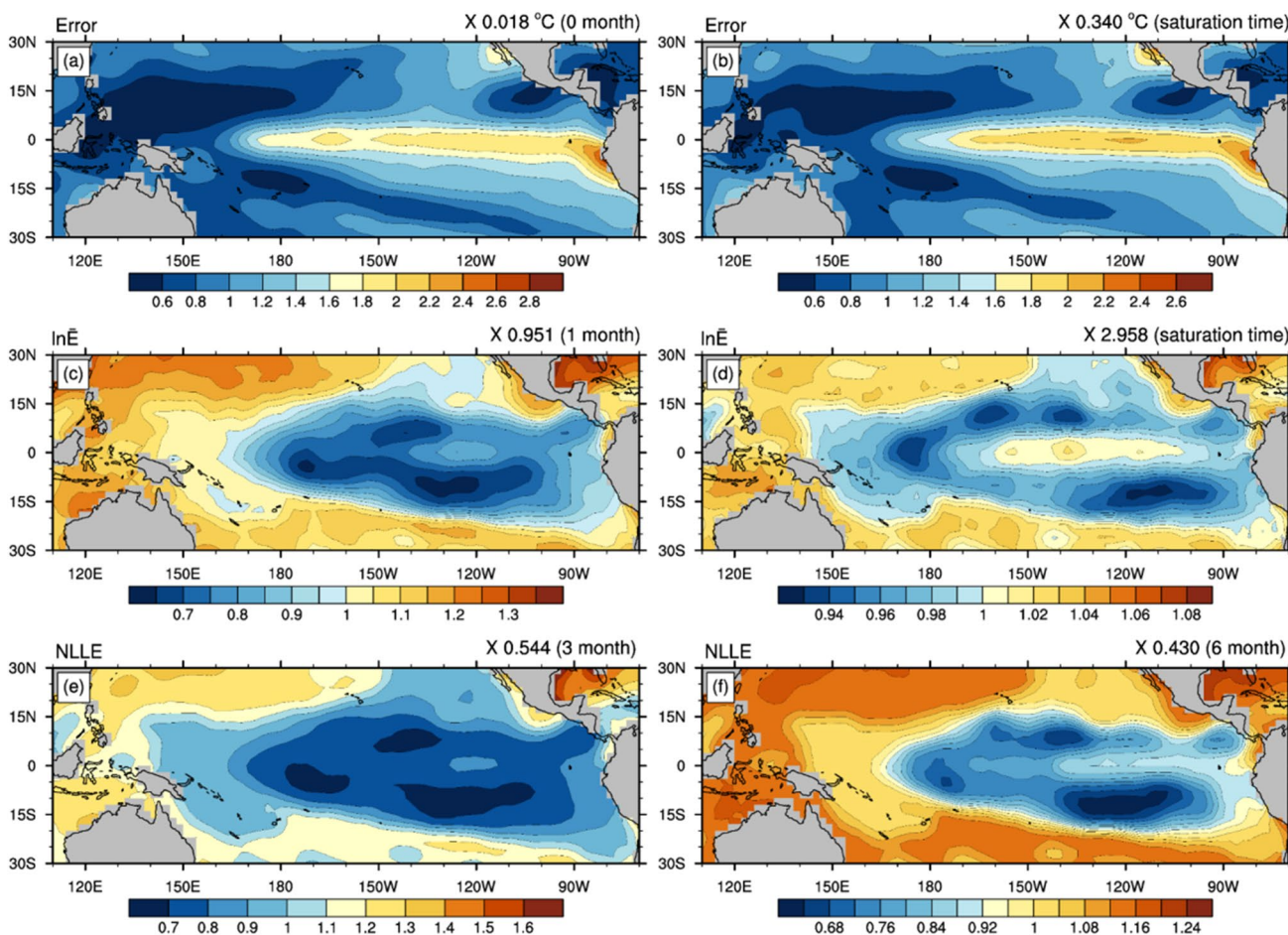


Fig. 6 Spatial distribution of error growth: **a** initial error at $\tau = 0$ month; **b** error at the saturation time; **c** RGIE at $\tau = 1$ month; **d** RGIE at the saturation time; **e** NLE at the evolution time of

3 months; **f** NLE at the evolutionary time of 6 months. Values shown are multiplied by the mean value of each variable shown in the top right corner of the diagram

is in the equatorial Pacific region near the east coast but that of the PL is in the central tropical Pacific. This implies that the absolute error does not fully determine the spatial pattern of PL values in the tropical Pacific. In fact, the error growth rate (NLE) and RGIE play important roles in the PL.

The RGIE is the key variable describing relative error growth and is used to calculate the PL of the dynamical system. Figure 6d displays the saturated RGIE values. As shown in Eq. (6), the saturated RGIE depends on the saturated and initial errors. The regions corresponding to large saturated error values often have large initial errors (Fig. 6a, b). Therefore, the distribution of the saturated RGIE will differ from the spatial pattern of the saturated or initial error. The saturated RGIE in the tropical Pacific ranges from 2.76 to 3.16—which corresponds to 0.93 to 1.08 times the mean saturated RGIE value (2.958) in the tropical Pacific—and has a horseshoe-shaped distribution: small values appear in the equatorial tropical Pacific around the dateline, and in the northeast and southeast Pacific near the equator, and are

surrounded by large saturated RGIE. Note that the spatial variation of the saturated RGIE is small (0.93 to 1.08 times the mean). A comparison with the spatial distribution of the mean PL (Fig. 1a) shows that regions with high saturated RGIE values have low PL, which suggests that the spatial distribution of saturated RGIE cannot explain the spatial pattern of the PL of SST in the tropical Pacific.

Meanwhile, the RGIE from 0 to 1 month also has a horseshoe shape (Fig. 6c), with low values in the central and eastern tropical Pacific and high values in the western tropical and subtropical Pacific. In contrast to the saturated RGIE that represents information signal intensity, the RGIE from 0 to 1 month is equivalent to the NLE in the evolutionary time of 1 month (from $\tau_i = 0$ month to $\tau_j = 1$ month) and represents the error growth over the first month. The values of RGIE from 0 to 1 month range from 0.6 to 1.3, suggesting the error grows to 1.8 (i.e. $e^{0.6}$) to 3.6 ($e^{1.3}$) times the initial error in 1 month. Thus, the high 0 to 1 month RGIE means faster forecast signal loss and low PL. Compared with the

spatial range of saturated RGIE (0.93/1.08) in the tropical Pacific, the spatial variation of the 0 to 1 month RGIE is larger (0.65/1.4), which indicates that the spatial pattern of NLE has a greater impact on the mean PL. Meanwhile, the spatial distribution of the 0 to 1 month RGIE is consistent with the pattern of mean PL in the tropical Pacific. Figure 6e and f display the mean error growth rate or NLE at 3 and 6 months over the period 1900–2015. The NLE for different evolution times has low values in the central and eastern tropical Pacific and high values in the western tropical and subtropical Pacific. A high value for NLE represents fast error growth over the given evolution time, thus corresponding to low PL, whereas low NLE corresponds to high PL. The NLE at evolution times of 3 (6) months has high spatial correlation coefficients with the PL pattern shown in Fig. 1a of -0.77 (-0.82), both of which reach the 90% confidence level. The similar pattern of the NLE and PL implies that the error growth rate is the key factor determining the spatial pattern of the PL.

The main factor affecting the spatial distribution of PL in the tropical Pacific is therefore error growth rate, whereas the RGIE at the time of saturation has little influence. The PL in different regions shows decadal variation; how does the error growth rate and saturated RGIE affect this decadal variability? As shown in Fig. 2, the Niño 3.4 and Niño 6

regions are the key regions where the ENSO dynamical systems develop, and their decadal variations, to an extent, represent the PL variation in the central/eastern tropical Pacific and the western tropical Pacific, respectively. Therefore, we first analyze the decadal variability of error growth of the Niño 3.4 and Niño 6 regions.

Figure 7 shows the decadal variation of saturated RGIE and error growth rate (NLE) from 1900 to 2015 in the Niño 3.4 and Niño 6 regions. The PL, RGIE, and NLE curves are normalized for better clarity. The NLE, saturated RGIE, and error also have obvious decadal variations. The RGIE at the saturated time of the Niño 3.4 region (blue–violet curve in Fig. 7a) has larger values in the 1900s, mid-1930s, mid-1960s, and 1980s to 2000s, which is generally consistent with the decadal variation of the PL of the Niño 3.4 region. In fact, the correlation coefficient between the PL and RGIE at the saturated time is 0.81 (passing the 90% confidence level), which indicates that the decadal variation of RGIE at the time of saturation plays an important role in the PL and explains almost 66% of the PL decadal variance of the Niño 3.4 region. The strong linkage between the decadal variation of saturated RGIE and that of the PL of the Niño 3.4 region agrees with results from the signal-to-noise method: highly saturated RGIE represents large signal intensity and high PL. However, the decline of PL around the 2000s appears

Fig. 7 Decadal variations of error growth variables for the **a** Niño 3.4 and **b** Niño 6 regions. The black curve is the PL in Niño regions, the blue–violet curve is RGIE at the saturation time, green represents the error relative growth rate (NLE) from 0 to 3 months, and deep-pink is the NLE from 0 to 6 months

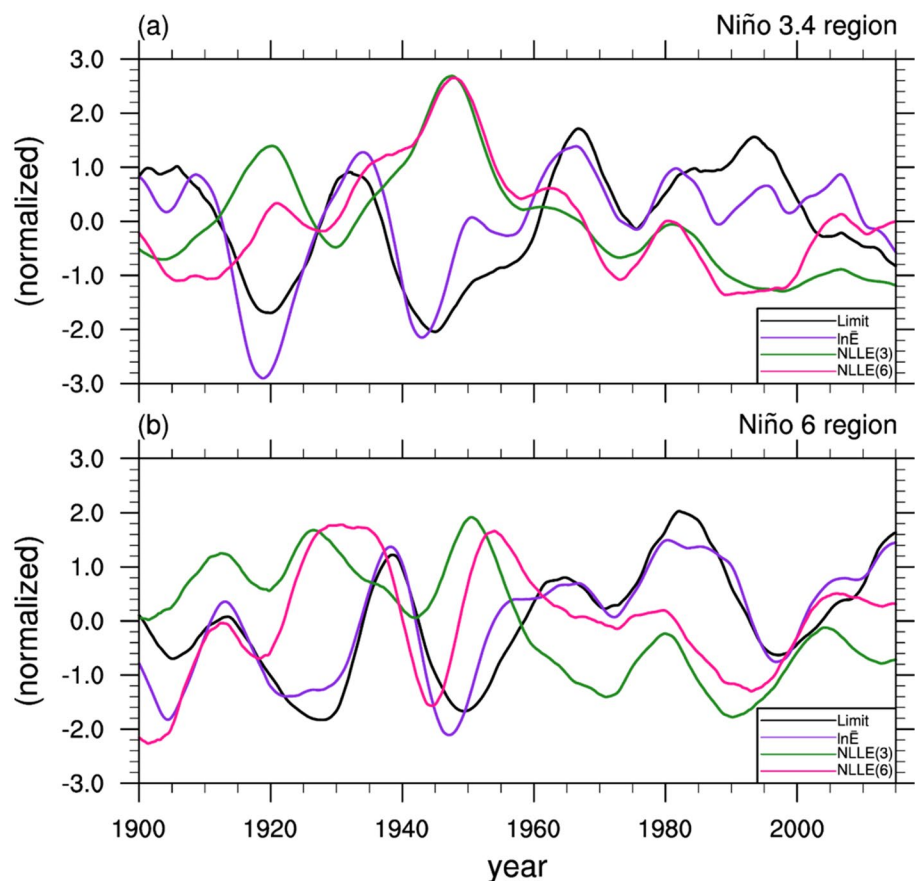
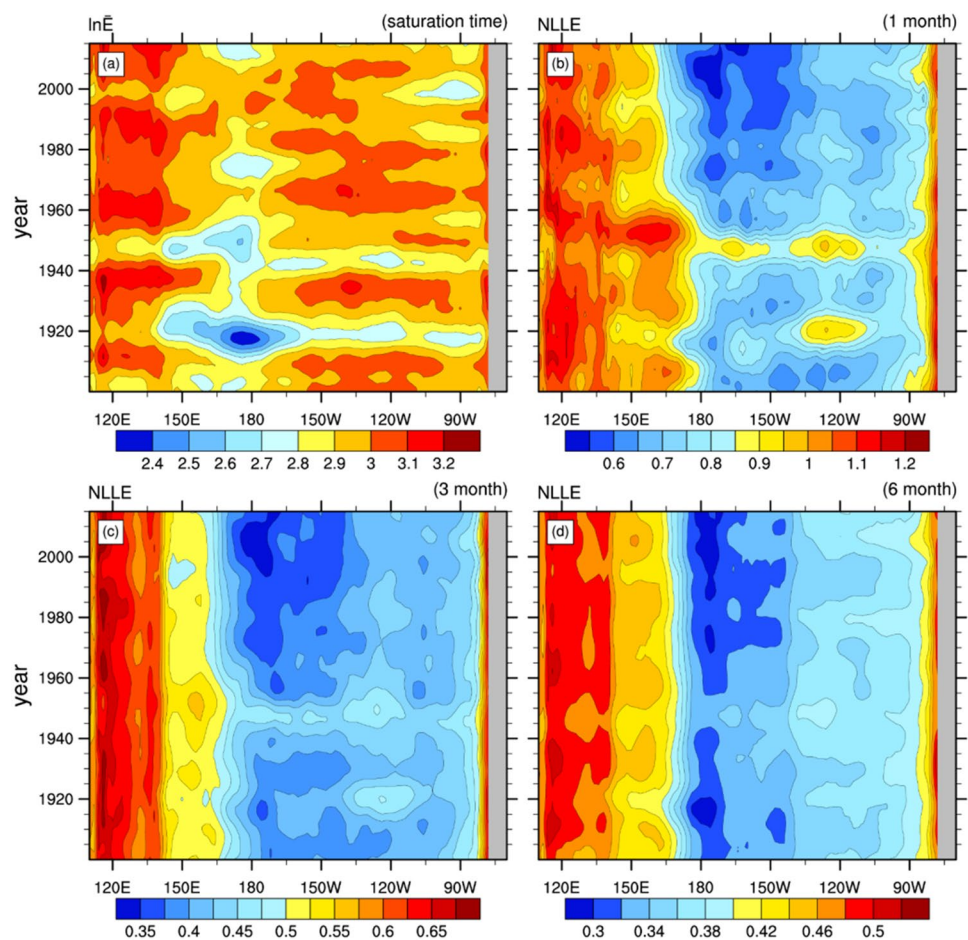


Fig. 8 Hovmöller diagram of the saturated RGIE (a), and NLE at the evolution times of b 1, c 3, and d 6 months, meridionally averaged from 5° S to 5° N in the tropical Pacific. The ordinate is the time from 1900 to 2015 and the abscissa is the longitude from 110° E to 70° W



to be an exception: the PL in the Niño 3.4 region started to decline from the mid-1990s to mid-2010s, but the saturated RGIE value grew consistently from the mid-1990s to mid-2000s. Therefore, other factors affect the decadal variability of the PL. Interestingly, the error growth rate, especially NLE (6) (that is, NLE over months 0 to 6), increased at the beginning of the mid-1990s, which contributes to the decline of the PL in the Niño 3.4 region from mid-1990s to mid-2010s, whereas the saturated RGIE value increased from the 2000s to mid-2000s. Thus, there is decadal variation in the error growth rate, which also has a large influence on the decadal variation of PL. The NLE over months 0 to 3 (NLE (3); forest-green curve in Fig. 7a) represents the mean error growth rate relative to an initial error during the evolution time of 3 months, and NLE (6) (deep-pink curve) represents the growth rate during the evolution time of 6 months. Clearly, high NLE corresponds to low PL, such as in the 1920s and 1950s, whereas low NLE corresponds to high PL, such as in the 1990s. The correlation coefficient between the PL and NLE (3) or NLE (6) is -0.70 or -0.63 , both of which the 90% confidence level, which confirms the important role of the error growth rate in the decadal variation of the PL.

Similar to the results for the Niño 3.4 region, the decadal variation of the PL of the Niño 6 region is consistent with the decadal variability of the RGIE at the time of saturation, represented by the black and blue–violet curves in Fig. 7b, respectively. The correlation coefficient between the PL and saturated RGIE is 0.90 (passing the 95% confidence level), which implies that high (low) RGIE at the time of saturation always gives a high (low) PL value. In addition, the error growth rate (NLE) has an opposing effect on the PL of the Niño 6 region. When NLE (3) and NLE (6) are high in the 1930s and mid-1950s, the PL is low. The decadal variation of PL in the Niño 6 region has a correlation coefficient of -0.66 , with NLE (3) that passes the 90% confidence level, as the fast error growth rate in the evolution time reduces the PL. We also calculate the correlation coefficient between the PL and NLE (6) in the Niño 6 region. The coefficient is -0.12 , which does not pass the 90% confidence level, as a result of the low PL value (~ 5 – 6 months) of the Niño 6 region. When the evolution time for NLE (6) is greater than the PL value, the error growth rate is less constrained. Compared with the relationship of the PL and RGIE or NLE of the Niño 3.4 region, the Niño 6 region shows a stronger correlation between the PL and

saturated RGIE, which implies that the decadal variation of PL depends more on the change of saturated RGIE of the Niño 6 region; this may result from the different physical mechanisms and greater atmospheric noise in the western tropical Pacific.

A more striking representation of error evolution at different longitudes is given by the Hovmöller diagram of the RGIE at the saturation time and NLE at different evolution times in Fig. 8. The NLE in the western Pacific is higher than that in the central and eastern Pacific, which is consistent with the result that PL is high in the central and eastern Pacific and low in the western Pacific. The decadal variation of saturated RGIE and NLE in the central and eastern Pacific differs from that in the western tropical Pacific. There are high values of saturated RGIE (Fig. 8a) in the 1900s, mid-1930s, and 1970s to 2000s for the central and eastern tropical Pacific and in the 1910s, mid-1930s, 1960s, 1990s, and mid-2010s for the western tropical Pacific, consistent with the decadal variability of PL. As shown in Fig. 8b, c, and d, the NLE patterns for these evolution times have similar decadal variation. The NLE of the central and eastern tropical Pacific is higher in the mid-1940s, which contributes to the lower PL. In the last decade, NLE (6) has increased at 165° W since the mid-1990s, which is consistent with the decadal decline of PL of the Niño 3.4 region.

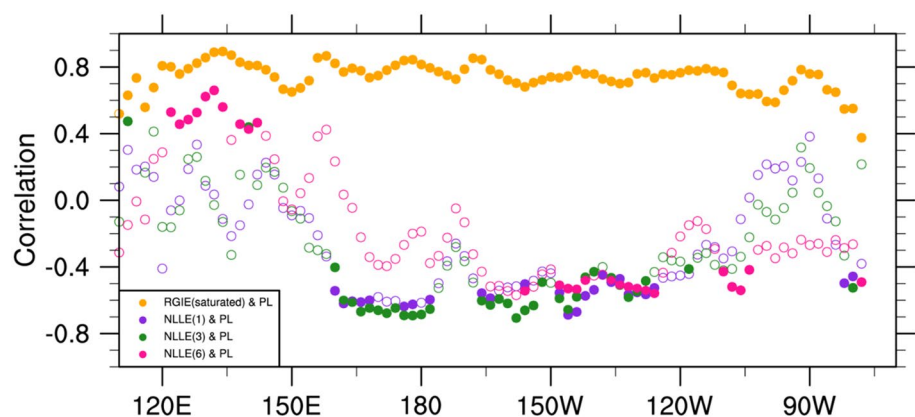
In terms of NLE theory, the decadal variation of saturated RGIE and NLE determines that of the PL, as shown in Figs. 7 and 8. To illustrate the role of NLE and saturated RGIE on the PL at different longitudes over the equatorial Pacific, we calculate the correlation coefficient between saturated RGIE or NLE at different evolution times and the PL at different longitudes in Fig. 9 (solid dots indicate coefficients that pass the 90% confidence level). The correlation coefficients between PL and saturated RGIE at different longitudes are always positive and pass the 90% confidence level, which indicates that the decadal variations of the PL are closely tied to the variation of saturated RGIE. The decadal variability of saturated RGIE can explain 60% of the decadal variation of PL in the equatorial Pacific. Compared

with the relationship between saturated RGIE and PL, the influence of NLE on the PL is more variable, varying with evolution time and longitude. The correlation coefficients between NLE and PL are significantly negative in the regions from 170° E to 125° W, which implies that high error growth rates lead to low values of the PL in the central and eastern tropical Pacific. In regions west of 165° E and east of 120° W, the relationship between NLE and PL is not significant, which may result from the role of stochastic physical processes such as atmospheric convection on SST in the region west of 165° E or offshore currents in the region east of 120° W. Interestingly, the PL in the regions west of 150° E has a significant positive correlation with NLE (6), which contradicts the idea that larger error growth rate decreases the PL. In fact, the region west of 150° E has low PL (lower than 6 months). Therefore, NLE (6), representing the error growth rate at the evolution time of 6 months, has some features in common with the variation of the saturated RGIE. Comparing the effect of the decadal variation of saturated RGIE and NLE on PL, we find that the decadal variation of the PL of SST in the tropical Pacific is caused by the change in saturated RGIE, while the error growth rate may affect some longitudinal regions.

3.3 Physical processes responsible for the decadal variation of the predictability limit

In the previous subsection, we analyzed the influence of error growth on the PL based on the NLE theory. However, it is not clear which physical processes affect the characteristics of error growth. As the primary source of seasonal-to-yearly climate variability in the tropical Pacific, ENSO events can be predicted up to three seasons in advance owing to the slow equatorial heat content recharge/discharge in the upper ocean (Cane and Zebiak 1985; Wang et al. 2017) that arises from the disequilibrium between zonal winds and WWV. The WWV, describing upper Pacific Ocean heat content, usually leads the ENSO SST evolution by a quarter of the ENSO period and acts as a useful predictor for ENSO

Fig. 9 Correlation coefficients between the decadal variation of error growth rate (NLE) or RGIE (saturated) and PL meridionally averaged from 5° S to 5° N in the tropical Pacific during the period 1900 to 2015. Solid dots indicate the correlation passes the 90% confidence level. The abscissa is the longitude from 110° E to 70° W

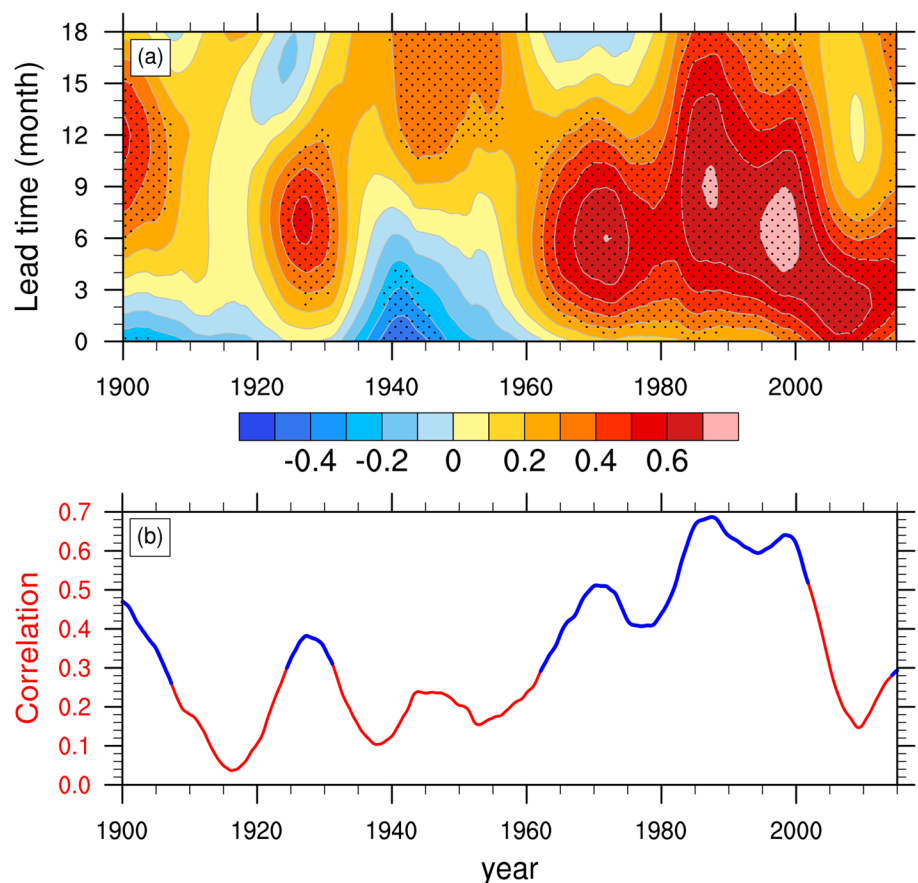


SST (McPhaden 2003). Therefore, WWV is an important predictability source for the SST field in the tropical Pacific. However, this phase-lag relationship between the WWV and ENSO SST varies on decadal timescales (Bunge and Clarke 2014); for example, the significant shift around 2000 when the lead time shortened from approximately two to three seasons to approximately one season (Bosc and Delcroix 2008; Neske and McGregor 2018; Neske et al. 2021). It seems plausible to link the variation of WWV–ENSO SST lead time and the decadal variability of SST predictability in the tropical Pacific because the upper ocean heat content provides the ocean memory for the long-lead predictability of SST in the tropical Pacific. From the viewpoint of NLE theory, the RGIE at the time of saturation and the error growth rate determine the PL of SST. Thus, we will explore how the RGIE (saturated) and error growth rate (NLE) are affected by the phase-lag relationship between the WWV and SST in the tropical Pacific. We focus here on the Niño 3.4 region, which is an important component of the ENSO dynamical system.

Figure 10a shows the phase-lag relationships between the WWV and the Niño 3.4 index from 1900 to 2015 within a $(9 \times 12 + 1)$ -month running window. We find pronounced decadal variability, which is consistent with the results of Zheng (2019). The correlation coefficients between WWV

and the Niño 3.4 index are low during the period 1940–1960 at lead times of 0 to 6 months. The phase-lag relationship has weakened at lead times of 6–9 months since the 2000s. Considering that the predictability barrier of ENSO is in spring (March to May, the spring predictability barrier; SPB) and ENSO's mature phase occurs in winter (December–February), there are between 7 (May–December) to 12 (March–February) months from spring to winter. Therefore, we calculate the mean correlation between the WWV index and Niño 3.4 at lead times of 7 to 12 months as Corr (WWV–Niño, 7–12) (red curve in Fig. 10b) to quantitatively characterize the relationship between WWV and the Niño 3.4 index and explore its effect on error growth and the PL. Corr (WWV–Niño, 7–12) represents the predictability information that WWV contributes to the Niño 3.4 index. When Corr (WWV–Niño, 7–12) is high, WWV can be regarded as a skillful predictor of the Niño 3.4 index, increasing the predictability limit of SST in the tropical Pacific. Consistent with the decadal variation shown in Fig. 10a, Corr (WWV–Niño, 7–12) (red curve in Fig. 10b) is high from the mid-1980s to 2000s, which corresponds to high PL (black curve in Fig. 7a), and is low from the 1940s to 1960s with low PL. Corr (WWV–Niño, 7–12) declines from the start of the twenty-first century with the decrease of PL in the Niño 3.4 region. The correlation coefficient between Corr

Fig. 10 **a** Correlation between the warm water volume (WWV) and Niño 3.4 index as a function of WWV lead month (vertical) and time (horizontal), within a $(9 \times 12 + 1)$ -month running window. The time shown is the middle month of each $(9 \times 12 + 1)$ -month window. A 9-year running average is applied to the correlation to reduce small fluctuations. **b** Average correlation between the WWV and Niño 3.4 at lead times of 7 to 12 months. The blue represents that at least half of the correlation coefficients used for averaging have passed the significant level of $\alpha = 0.1$



(WWV-Niño, 7–12) and PL is 0.69 (exceeding the 90% confidence level), which supports the important role of the phase-lag relationships between the WWV and the Niño 3.4 index in the decadal variability of PL.

From the perspective of error growth, the variation of the phase-lag relationships between WWV and Niño 3.4 index has an impact on the saturated RGIE and error growth rate. The decadal variation of Corr (WWV-Niño, 7–12) is consistent with the saturated RGIE. In periods with strong phase-lag relationships between WWV and Niño such as in the 1900s, 1930s, 1970s, and 1990s, saturated RGIE is larger, which promotes high PL. Saturated RGIE is relatively low when Corr (WWV-Niño, 7–12) is lower, such as in the 1920s and 1950s. In fact, the correlation between Corr (WWV-Niño, 7–12) and saturated RGIE (blue–violet curve in Fig. 7a) is 0.44, which also passes the 90% confidence level under the effective degrees of freedom described in Sect. 2.1. Meanwhile, NLE at lead times of 1, 3, and 6 months is more rapid when Corr (WWV-Niño, 7–12) is low, such as during the 1920s and 1950s. When Corr (WWV-Niño, 7–12) is high, NLE is lower and the predictability limit is larger, such as from the 1980s to 2000s, because with high correlation, WWV can provide more information to predict SST and reduce the error growth rate. Further confirmation is provided by the correlation between Corr (WWV-Niño, 7–12) and NLE (3) (coefficient is -0.60), and the correlation between Corr (WWV-Niño, 7–12) and NLE (6) is -0.55 , both of which pass the 90% confidence level.

Based on the correlation between WWV and SST in the Niño 3.4 region, we calculate the composite results of NLE, saturated RGIE, and error for composites of high (>0.3) and low (<0.3) correlation. For early lead times (<5 months), the error growth rate (NLE) is lower where the correlation between WWV and Niño is higher. In particular, the NLE difference between the high and low correlation periods reaches 0.1 at a lead time of 1 month, meaning that the error growth rate of SST in the low correlation period is 1.10 ($e^{0.1}$) times that in the high correlation period. At lead times of 1–5 months, the error growth rate contributes to the difference of RGIE between high and low correlation periods (Fig. 11b). The value of RGIE in the low correlation period is greater than that in the high correlation period, which reduces the PL. However, the high RGIE in the low period decreases with increasing lead time. Unlike the RGIE for early lead times, the saturated RGIE of the high correlation period is higher than that of the low correlation period (Fig. 12b), which shows the high predictability signal in the high correlation period. Thus, the slow growth of RGIE in early lead times and the high value of RGIE at the saturated time together contribute to the high PL in the high correlation period and low PL in the low correlation period. The composite error as a function of lead time in the high and low correlation periods is also shown in Fig. 11c. The faster error

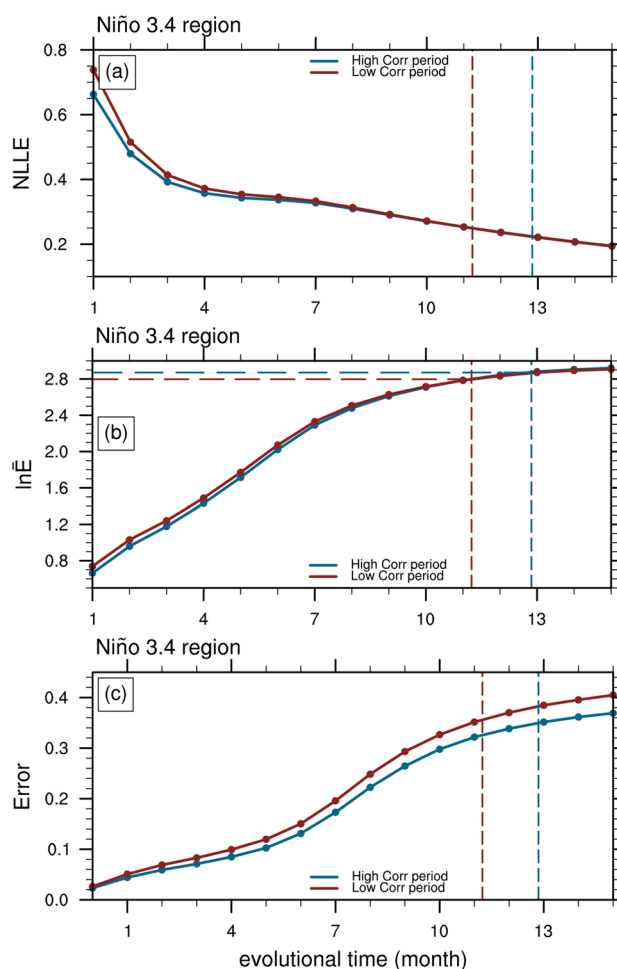


Fig. 11 Compositing error growth lines based on the correlation coefficient between the Niño 3.4 index and WWV index. The brown lines represent the low correlation period and deep-sky-blue lines the high correlation period

growth rate at early lead times gives a larger error in the low correlation period than in the high correlation period. With increasing lead time, the error in the low correlation period is always larger, which corresponds to low PL.

The relationship between WWV and the Niño 3.4 index not only affects the PL in the Niño 3.4 region, but also plays an important role in the PL of SST in other regions of the tropical Pacific. Figure 12 displays the spatial field of the difference of the PL, saturated RGIE and NLE at different evolution times between the high and low correlation periods. Compared to the PL pattern in low correlation periods, the PL of SST in high correlation periods is larger over almost the entire tropical Pacific except the tropical Pacific warm pool. The maximum difference of PL reaches 3 months near the dateline and 165°W in the equatorial Pacific (Fig. 12a). The saturated RGIE in the high correlation period has larger values than in the low correlation period over almost all of the tropical Pacific (Fig. 12b), which indicates that stronger

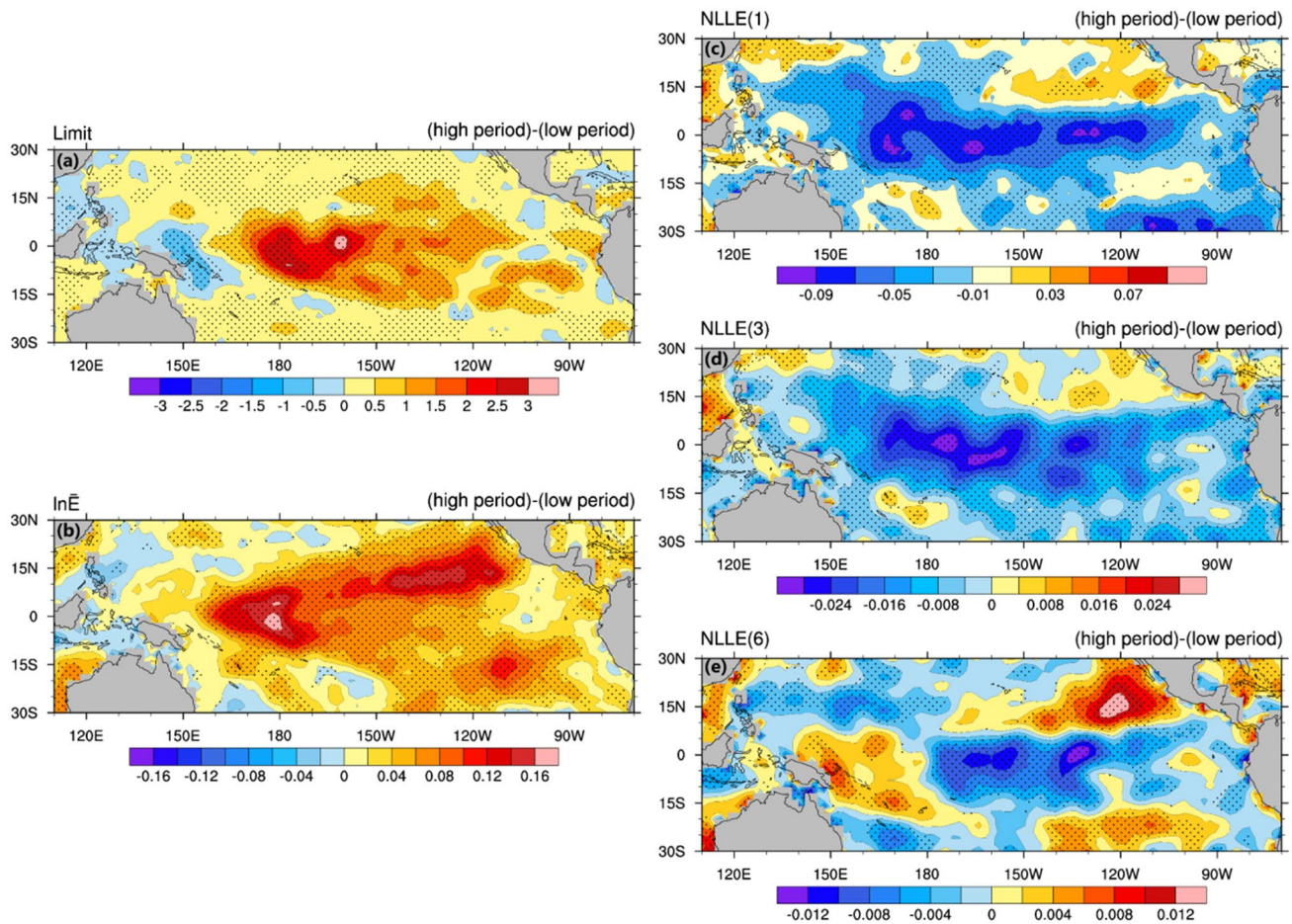


Fig. 12 Composite differences between high and low correlation periods of the **a** predictability limit, **b** RGIE ($\ln \bar{E}$) at the saturated time, and NLE at lead times of **c** 1 month, **d** 3 months, and **e** 6 months. The dotted region passes the 90% confidence level

forecast signal contributes to the high PL. In addition to the maximum difference of saturated RGIE at the dateline in the equatorial Pacific being similar to the difference pattern of the PL, the saturated RGIE also has an extreme center in the northeast Pacific where the difference of PL is small. The NLE represents error growth rate, whose pattern changes with evolution time. The NLE at a lead time of 1 month (Fig. 12c) is smaller in the equatorial Pacific but larger in the northeast Pacific in the high correlation period than in the low correlation period. The difference pattern of NLE for an evolution time of 3 months (Fig. 12d) is similar to the pattern of NLE at an evolution time of 1 month. The larger NLE in the high correlation period in the northeast Pacific reduces the effect of increasing PL caused by the increase of saturated RGIE, so that the PL of the northeast Pacific increases less during the high correlation period. Unlike the difference pattern of NLE between the high and low correlation periods at evolution times of 1 and 3 months, the NLE (6) in the equatorial west Pacific is larger in the high

correlation period than in the low correlation period, leading to a low PL in the west Pacific warm pool.

4 Conclusions and discussion

In this paper, we have investigated the mean PL of SST and its decadal variation in the tropical Pacific from 1900 to 2015 using observational SST data. The average PL in the tropical Pacific from 1900 to 2015 is high in the central and eastern Pacific (over 13 months) and is lower than 7 months in the western tropical Pacific. There are decadal variations in the PL in the tropical Pacific that can be as large as 2 months as measured by the standard deviation of the PL. These decadal variations differ between the western and central/eastern Pacific, as shown by the time series of PL in the different key Niño regions: the decadal variation is larger in the Niño 3.4 region than in the Niño 6 region. The Niño 3.4 region, representative of the central/eastern Pacific, has high PL in the 1900s, mid-1930s, mid-1960s, and mid-1990s

and low PL in the 1920s, mid-1940s, and mid-2010s. The PL of the western tropical Pacific can be represented by the PL of the Niño 6 region and is higher in the mid-1910s, 1940s, 1980s, and mid-2010s and lower in the 1930s, 1950s, and mid-1990s. The decadal variations of PL in the central and eastern tropical Pacific are consistent and are well represented by those in the Niño 3.4 region; they differ from those in the western tropical Pacific, represented by the Niño 6 region. The difference between the decadal variability of PL in the central/eastern tropical Pacific and that in the western tropical Pacific is more obvious in the Hovmöller diagram of PL. The lower PL in the western Pacific is probably ascribed to the local air-sea interaction. There is also a low PL in the eastern tropical Pacific near the coast, which may result from the influence of offshore currents. The whole equatorial Pacific also shows more obvious decadal variation.

With the NLLE method, the PL is determined by the error growth rate and saturated RGIE. Thus, we investigated their spatial pattern and decadal variability in the framework of error growth dynamics. We found that the main factor affecting the spatial distribution of mean PL in the tropical Pacific is error growth rate (NLLE) when the RGIE at the saturated time has little influence. Regions with low error growth rate have higher PL, and vice versa. Note that the spatial pattern of actual error is clearly different from that of the mean PL, which suggests that the traditional method of estimating PL by a constant mean square error is inappropriate. The different PLs in the western Pacific and central/eastern Pacific may result from the different atmospheric and oceanic dynamical processes. The oceanic processes are slow, which favors the longer PL in the central/eastern Pacific. SST in the western Pacific is affected by atmospheric activity, which introduces more atmospheric noise to SST and reduces the PL of SST.

To investigate the decadal variation of PL, we chose the average of the Niño 3.4 region to represent the central/eastern Pacific and that of the Niño 6 region as the western tropical Pacific and analyzed their decadal variation of saturated RGIE and error growth rate (NLLE). The RGIE at the saturated time of the Niño 3.4 region has larger values in the 1900s, mid-1930s, mid-1960s, and 1980s to 2000s, which is overall consistent with the decadal variation of the PL of the Niño 3.4 region. The high correlation coefficients show that the decadal variation of saturated RGIE plays an important role in the PL and explains almost 66% of the PL decadal variance of Niño 3.4 region. In addition, there is decadal variation of the error growth rate, which also has a big influence on the decadal variation of PL. In particular, the NLLE at the evolution time of 6 months has increased since the mid-1990s, which contributes to the decline of the PL in the Niño 3.4 region from the mid-1990s. Compared with the relationship between the PL and RGIE or NLLE of the Niño 3.4 region, there is stronger correlation between the PL and

saturated RGIE in the Niño 6 region, which implies that the decadal variation of PL is more dependent on the change of saturated RGIE in the Niño 6 region. This may result from the different physical mechanisms and greater atmospheric noise in the western tropical Pacific. Comparing the roles of the decadal variation of saturated RGIE and NLLE in the PL, we find that the decadal variation of the PL of SST in the tropical Pacific is due to the change of saturated RGIE, whereas the error growth rate may have an effect in some longitudinal regions of the equatorial Pacific.

The SST on a seasonal scale in the tropical Pacific is affected by the ocean heat capacity, for example, as described by the ENSO recharge–discharge theory. Further analyses indicate that the interdecadal variation in predictability is closely related to the interdecadal variation of the relationship between WWV and SST. From the perspective of error growth, the variation of the phase-lag relationships between WWV and Niño has an impact on the saturated RGIE and error growth rate. In the period with high phase-lag relationships between WWV and Niño, saturated RGIE is larger and NLLE is lower for lead times of 3 and 6 months, which favors high PL, such as in the 1900s, 1930s, 1970s, and 1990s. When the correlation between WWV and SST is lower, the saturated RGIE is relatively low and NLLE at lead times of 3 and 6 months is higher, such as in the 1920s and 1950s. A possible explanation is that the high correlation between WWV and Niño suggests a greater contribution of the slowly varying oceanic signal to the evolution of SST, leading to a longer cycle and stronger intensity of ENSO, which corresponds to high RGIE at the saturated time and increases the PL. The PL behavior in the western Pacific is not well explained by the WWV-SST relationship because of active atmospheric convection. In this paper, we display the decadal variability of seasonal PL in the tropical/subtropical PL over the period from 1900 to 2015 based on observation/analysis data, which increases our understanding of ENSO. The current climate model has some shortcomings in the simulation of SST, thus the performance of the climate model needs to be evaluated in the predictability, which is helpful to improve the capacity of the model.

Acknowledgements We acknowledge the support of the Center for High Performance Computing and System Simulation, Qingdao Pilot National Laboratory for Marine Science and Technology.

Funding This work was jointly supported by the National Natural Science Foundation of China (NSFC, 42005049 and 42130607) projects, Shandong Natural Science Foundation Project (ZR2020QD056 and ZR2019ZD12), Postdoctoral Science Foundation of China (2020M680094) and Fundamental Research Funds for the Central Universities (201962009, 202013031). We acknowledge the support of the Center for High Performance Computing and System Simulation, Qingdao Pilot National Laboratory for Marine Science and Technology.

Data availability statement Monthly sea surface temperature (SST) dataset is available at <https://www.esrl.noaa.gov/psd/data/gridded/data.noaa.ersst.v5.html>. Ocean variables are available at http://apdrc.soest.hawaii.edu/datadoc/soda_2.2.4.php and <https://psl.noaa.gov/data/gridded/data.godas.html>.

Declarations

Conflicts of interest The authors declare no competing interests.

Code availability Computer code used for the analysis was written in NCL, all types of figures that occur in this study can be found in NCL application examples (available online at <https://www.ncl.ucar.edu/Applications/>). More specific codes in this study are available to readers upon request.

Open Access This article is licensed under a Creative Commons Attribution 4.0 International License, which permits use, sharing, adaptation, distribution and reproduction in any medium or format, as long as you give appropriate credit to the original author(s) and the source, provide a link to the Creative Commons licence, and indicate if changes were made. The images or other third party material in this article are included in the article's Creative Commons licence, unless indicated otherwise in a credit line to the material. If material is not included in the article's Creative Commons licence and your intended use is not permitted by statutory regulation or exceeds the permitted use, you will need to obtain permission directly from the copyright holder. To view a copy of this licence, visit <http://creativecommons.org/licenses/by/4.0/>.

References

- Balmaseda MA, Davey MK, Anderson DLT (1995) Decadal and seasonal dependence of ENSO prediction skill. *J Clim* 8:2705–2715. [https://doi.org/10.1175/1520-0442\(1995\)008%3c2705:DAS-DOE%3e2.0.CO;2](https://doi.org/10.1175/1520-0442(1995)008%3c2705:DAS-DOE%3e2.0.CO;2)
- Barnston AG, Tippett MK, L'Heureux ML, Li S, DeWitt DG (2012) Skill of real-time seasonal ENSO model predictions during 2002–11: is our capability increasing? *Bull Am Meteor Soc* 93:631–651. <https://doi.org/10.1175/bams-d-11-00111.1>
- Behringer DW (2007) 3.3 The Global Ocean Data Assimilation System (GODAS) at NCEP. In: Proceedings of the 11th symposium on integrated observing and assimilation systems for the atmosphere, oceans, and land surface
- Bosc C, Delcroix T (2008) Observed equatorial Rossby waves and ENSO-related warm water volume changes in the equatorial Pacific Ocean. *J Geophys Res Oceans* 113
- Bretherton CS, Widmann M, Dymnikov VP, Wallace JM, Bladé I (1999) The effective number of spatial degrees of freedom of a time-varying field. *J Clim* 12:1990–2009
- Bunge L, Clarke AJ (2014) On the warm water volume and its changing relationship with ENSO. *J Phys Oceanogr* 44:1372–1385
- Cai WJ, McPhaden MJ, Grimm AM, Rodrigues RR, Taschetto AS et al (2020) Climate impacts of the El Niño-southern oscillation on South America. *Nat Rev Earth Environ* 1:215–231. <https://doi.org/10.1038/s43017-020-0040-3>
- Cane MA, Zebiak SE (1985) A theory for El Niño and the Southern Oscillation. *Science* 228:1085–1087
- Castro SL, Wick GA, Jackson DL, Emery WJ (2008) Error characterization of infrared and microwave satellite sea surface temperature products for merging and analysis. *J Geophys Res Oceans* 113(C3)
- Chen D, Cane MA (2008) El Niño prediction and predictability. *J Comput Phys* 227:3625–3640. <https://doi.org/10.1016/j.jcp.2007.05.014>
- Chen D, Cane MA, Kaplan A, Zebiak SE, Huang D (2004) Predictability of El Niño over the past 148 years. *Nature* 428:733–736. <https://doi.org/10.1038/nature02439>
- Chen BH, Li JP, Ding RQ (2006) Nonlinear local Lyapunov exponent and atmospheric predictability research. *Sci China Ser D Earth Sci* 49:1111–1120. <https://doi.org/10.1007/s11430-006-1111-0>
- Chen D, Lian T, Fu C, Cane MA, Tang Y (2015) Strong influence of westerly wind bursts on El Niño diversity. *Nat Geosci* 8:339–345
- Ding RQ, Li JP (2007) Nonlinear finite-time Lyapunov exponent and predictability. *Phys Lett A* 364:396–400. <https://doi.org/10.1016/j.physleta.2006.11.094>
- Ding RQ, Li JP, Ha KJ (2008) Trends and interdecadal changes of weather predictability during 1950s–1990s. *J Geophys Res Atmos* 113:1–11. <https://doi.org/10.1029/2008jd010404>
- Ding RQ, Li JP, Zheng F, Feng J, Liu DQ (2016) Estimating the limit of decadal-scale climate predictability using observational data. *Clim Dyn* 46:1563–1580. <https://doi.org/10.1007/s00382-015-2662-6>
- Duan W, Mu M (2018) Predictability of El Niño-southern oscillation events. *Oxford research encyclopedia of climate science*. Oxford University Press, Oxford
- Duan W, Mu M, Duan W, Mu M (2018) Predictability of El Niño-southern oscillation events. Oxford University Press, Oxford, pp 1–39
- Eckmann JP, Ruelle D (1985) Ergodic theory of chaos and strange attractors. *Rev Mod Phys* 57:617–656. <https://doi.org/10.1103/RevModPhys.57.617>
- Hou ZL, Li JP, Ding RQ, Feng J, Duan WS (2018a) The application of nonlinear local Lyapunov vectors to the Zebiak-Cane model and their performance in ensemble prediction. *Climate Dynamics* 51(1–2):283–304. <https://doi.org/10.1007/s00382-017-3920-6>
- Hou ZL, Li JP, Ding RQ, Karamperidou C, Duan W, Liu T, Feng J (2018b) Asymmetry of the predictability limit of the warm ENSO phase. *Geophys Res Lett* 45:7646–7653
- Hou ZL, Li JP, Zuo B (2021) Correction of monthly SST forecasts in CFSv2 using the local dynamical analog method. *Weather Forecast* 36:843–858. <https://doi.org/10.1175/Waf-D-20-0123.1>
- Hou ZL, Zuo B, Zhang S, Huang F, Ding R, Duan WS, Li JP (2020) Model forecast error correction based on the local dynamical analog method: an example application to the ENSO forecast by an intermediate coupled model. *Geophys Res Lett* 47:e2020GL088986
- Huang B, Thorne PW, Banzon VF, Boyer T, Chepurin G et al (2017) Extended reconstructed sea surface temperature, version 5 (ERSSTv5): upgrades, validations, and intercomparisons. *J Clim* 30:8179–8205
- Jin F-F (1997) An equatorial ocean recharge paradigm for ENSO. Part I: conceptual model. *J Atmos Sci* 54:811–829
- Kaplan A, Cane MA, Kushnir Y, Clement AC, Blumenthal MB, Rajagopalan B (1998) Analyses of global sea surface temperature 1856–1991. *J Geophys Res Oceans* 103(C9):18567–18589. <https://doi.org/10.1029/97JC01736>
- Karamperidou C, Cane MA, Lall U, Wittenberg AT (2014) Intrinsic modulation of ENSO predictability viewed through a local Lyapunov lens. *Clim Dyn* 42:253–270
- Kirtman BP, Schopf PS (1998) Decadal variability in ENSO predictability and prediction. *J Clim* 11:2804–2822
- Kirtman BP (2003) The COLA anomaly coupled model: ensemble ENSO prediction. *Monthly Weather Rev* 131: 2324–2341. DOI: [https://doi.org/10.1175/1520-0493\(2003\)131<2324:Tcacme>2.0.Co;2](https://doi.org/10.1175/1520-0493(2003)131<2324:Tcacme>2.0.Co;2)
- Kumar A, Hu ZZ, Jha B, Peng PT (2017) Estimating ENSO predictability based on multi-model hindcasts. *Clim Dyn* 48:39–51. <https://doi.org/10.1007/s00382-016-3060-4>

- Lacarra J-F, Talagrand O (1988) Short-range evolution of small perturbations in a barotropic model. *Tellus A* 40:81–95
- Latif M, Anderson D, Barnett T, Cane M, Kleeman R et al (1998) A review of the predictability and prediction of ENSO. *J Geophys Res Oceans* 103:14375–14393. <https://doi.org/10.1029/97jc03413>
- Li JP, Ding RQ (2011) Temporal-spatial distribution of atmospheric predictability limit by local dynamical analogs. *Mon Weather Rev* 139:3265–3283. <https://doi.org/10.1175/Mwr-D-10-05020.1>
- Li JP, Ding RQ (2013) Temporal-spatial distribution of the predictability limit of monthly sea surface temperature in the global oceans. *Int J Climatol* 33:1936–1947. <https://doi.org/10.1002/joc.3562>
- Li JP, Ding RQ (2015) Weather forecasting: seasonal and interannual weather prediction. *Encycl Atmos Sci Second Ed* 6:303–312. <https://doi.org/10.1016/B978-0-12-382225-3.00463-1>
- Li JP, Wang SH (2008) Some mathematical and numerical issues in geophysical fluid dynamics and climate dynamics. *Commun Comput Phys* 3:759–793
- Li JP, Sun C, Jin FF (2013) NAO implicated as a predictor of Northern Hemisphere mean temperature multidecadal variability. *Geophys Res Lett* 40:5497–5502
- Li JP, Feng J, Ding RQ (2018) Attractor radius and global attractor radius and their application to the quantification of predictability limits. *Clim Dyn* 51:2359–2374. <https://doi.org/10.1007/s00382-017-4017-y>
- Li JP, Zheng F, Sun C, Feng J, Wang J (2019) Pathways of influence of the Northern Hemisphere mid-high latitudes on East Asian climate: a review. *Adv Atmos Sci* 36:902–921. <https://doi.org/10.1007/s00376-019-8236-5>
- Li JP, Xie TJ, Tang XX, Wang H, Sun C et al (2021) Influence of the NAO on wintertime surface air temperature over East Asia: multidecadal variability and decadal prediction. *Adv Atmos Sci*. <https://doi.org/10.1007/s00376-021-1075-1>
- Lopez H, Kirtman BP (2014) WWBs, ENSO predictability, the spring barrier and extreme events. *J Geophys Res Atmos* 119:10114–110138
- Lorenz EN (1969) Atmospheric predictability as revealed by naturally occurring analogues. *J Atmos Sci* 26:636–646. [https://doi.org/10.1175/1520-0469\(1969\)26%3c636:Aparbn%3e2.0.Co;2](https://doi.org/10.1175/1520-0469(1969)26%3c636:Aparbn%3e2.0.Co;2)
- McPhaden MJ (2003) Tropical Pacific Ocean heat content variations and ENSO persistence barriers. *Geophys Res Lett* 30
- Meinen CS, McPhaden MJ (2000) Observations of warm water volume changes in the equatorial Pacific and their relationship to El Niño and La Niña. *J Clim* 13:3551–3559
- Mu M, Duan WS (2003) A new approach to studying ENSO predictability: conditional nonlinear optimal perturbation. *Chin Sci Bull* 48:1045–1047. <https://doi.org/10.1360/02wd0389>
- Neske S, McGregor S (2018) Understanding the warm water volume precursor of ENSO events and its interdecadal variation. *Geophys Res Lett* 45:1577–1585
- Neske S, McGregor S, Zeller M, Dommenges D (2021) Wind spatial structure triggers ENSO's oceanic warm water volume changes. *J Clim* 34:1985–1999. <https://doi.org/10.1175/Jcli-D-20-0040.1>
- Penland C, P. D., Sardeshmukh, (1995) The optimal growth of tropical sea surface temperature anomalies. *J Clim* 8(8):1999–2024
- Pyper BJ, Peterman RM (1998) Comparison of methods to account for autocorrelation in correlation analyses of fish data. *Can J Fish Aquat Sci* 55:2127–2140
- Rayner NA, Parker DE, Horton EB, Folland CK, Alexander LV, Rowell DP, Kent EC, Kaplan A (2003) Global analyses of sea surface temperature, sea ice, and night marine air temperature since the late nineteenth century. *J Geophys Res Atmos* 108(D14). <https://doi.org/10.1029/2002JD002670>
- Reynolds RW, Smith TM (1994) Improved global sea surface temperature analyses using optimum interpolation. *J Clim* 7(6):929–948
- Reynolds RW, Smith TM, Liu CC, Chelton DB, Casey KS, Schlax MG (2007) Daily high-resolution-blended analyses for sea surface temperature. *J Clim* 20(22):5473–5496. <https://doi.org/10.1175/2007JCLI1824.1>
- Tang YM, Deng ZW, Zhou XB, Cheng YJ, Chen D (2008) Interdecadal variation of ENSO predictability in multiple models. *J Clim* 21:4811–4833. <https://doi.org/10.1175/2008jcli2193.1>
- Timmermann A, An SI, Kug JS, Jin FF, Cai W (2018) El Niño-southern oscillation complexity. *Nature* 559:535–545. <https://doi.org/10.1038/s41586-018-0252-6>
- Wang CZ (2018) A review of ENSO theories. *Natl Sci Rev* 5:813–825. <https://doi.org/10.1093/nsr/nwy104>
- Wang CZ, Weisberg RH, Virmani JI (1999) Western Pacific interannual variability associated with the El Niño-Southern oscillation. *J Geophys Res Oceans* 104:5131–5149
- Wang CZ, Deser C, Yu J (2017) El Niño and Southern oscillation (ENSO): a review. *Coral Reefs Eastern Trop Pac* 85–106
- Wyrki K (1985) Water displacements in the Pacific and the genesis of El Niño cycles. *J Geophys Res Oceans* 90:7129–7132
- Xie SP, Kosaka Y, Du Y, Hu KM, Chowdary J, Huang G (2016) Indo-western Pacific ocean capacitor and coherent climate anomalies in post-ENSO summer: a review. *Adv Atmos Sci* 33:411–432. <https://doi.org/10.1007/s00376-015-5192-6>
- Yeh SW, Cai WJ, Min SK, McPhaden MJ, Dommenges D (2018) ENSO atmospheric teleconnections and their response to greenhouse gas forcing. *Rev Geophys* 56:185–206. <https://doi.org/10.1002/2017rg000568>
- Zebiak SE, Cane MA (1987) A model El Niño-southern oscillation. *Monthly Weather Review*, 2262–2278
- Zhang W, Jiang F, Stuecker MF, Jin FF, Timmermann A (2021) Spurious North tropical atlantic precursors to El Niño. *Nat Commun* 12:3096. <https://doi.org/10.1038/s41467-021-23411-6>
- Zhao M, Hendon HH, Alves O, Liu GQ, Wang GM (2016) Weakened eastern Pacific El Niño predictability in the early twenty-first century. *J Clim* 29:6805–6822. <https://doi.org/10.1175/Jcli-D-15-0876.1>
- Zheng F, Fang XH, Zhu J, Yu JY, Li XC (2016) Modulation of Bjerknes feedback on the decadal variations in ENSO predictability. *Geophys Res Lett* 43:12560–12568. <https://doi.org/10.1002/2016gl071636>

Publisher's Note Springer Nature remains neutral with regard to jurisdictional claims in published maps and institutional affiliations.